· Article · Advances in Polar Science
doi: 10.13679/j.advps.2017.3.00171 September 2017 Vol. 28 No. 3: 171–184

Mechanisms associated with winter intraseasonal extreme sea ice extent in the Weddell Sea

Fabio Ullmann Furtado de LIMA[1*] & Leila M. V. CARVALHO[2]

[1] Centro de Ensino Superior da Foz do Itajaí—Univ. do Estado de Santa Catarina (UDESC), Balneario Camboriu—SC 88330-668, Brazil;
[2] Dept. of Geography and Earth Research Institute, University of California Santa Barbara, CA 93106-9010, USA

Received 24 February 2017; accepted 30 May 2017

Abstract Previous studies have shown evidence of atmospheric extratropical wave trains modulating sea ice area in the Weddell and Amundsen/Bellingshausen seas on intraseasonal time-scales (20–100 d). Here we investigate mechanisms relating intraseasonal extreme sea ice extent and Ekman layer dynamics with emphasis on the Weddell Sea. This study extends from 1989 to 2013 and focuses on the winter season. Wind stress τ is calculated with winds from the Climate Forecast System reanalysis (CFSR) to evaluate momentum transfer between the atmosphere and the Ekman layer. Lag-composites of the anomalies of Ekman transport and the Ekman pumping indicate that divergence of mass in the Ekman layer and upwelling lead the occurrence of extreme sea ice contraction on intraseasonal time-scales in the Weddell Sea. Opposite conditions (i.e., convergence of the mass and downwelling) lead extreme sea ice expansion on intraseasonal time-scales. This study suggests that the Ekman pumping resulting from the anomalous wind stress on intraseasonal time-scales can transport these warmer waters to the surface contributing to sea ice melting. Additionally, high resolution sea ice fraction and ocean currents obtained from satellite and in situ data are used to investigate in detail mechanisms associated with persistent extreme sea ice expansion and contraction on intraseasonal time-scales. These case studies reveal that atmospheric circumpolar waves on intraseasonal time-scales can induce contrasting anomalies of about ±20% in sea ice concentration at the Weddell and western Antarctica Peninsula margins within less than 30 d. This study shows that extreme anomalies in sea ice may lag between 5–25 d (1–5 pentads) the ocean-atmospheric forcing on intraseasonal time-scales.

Keywords **sea ice extent, intraseasonal time-scales, Ekman layer dynamics**

Citation: Lima F U F, Carvalho L M V. Mechanisms associated with winter intraseasonal extreme sea ice extent in the Weddell Sea. Adv Polar Sci, 2017, 28(3): 171–184, doi: 10.13679/j.advps.2017.3.00171

1 Introduction

The influence of global climate on Antarctic sea ice has been well documented (e.g, Raphael, 2007; Gillet and Thompson, 2003; Yuan and Martison, 2000). Many studies have shown the impact of atmospheric circulation at midlatitudes on sea ice extent. The majority of these studies relate the intensity of westerly winds and local winds to Antarctic sea ice variability (Holland and Kwok, 2012; Gillet and Thompson, 2003; Wunsch, 1998; Streten and Pike, 1980; Gordon et al., 1977). The Southern Hemisphere westerly winds have been strengthening and shifting poleward since 1950s, likely induced by global warming and stratospheric ozone-depletion (particularly in the summer) (Spence et al., 2014; Thompson et al., 2011; Fyfe et al., 2007; Arblaster and Meehl, 2006). Spence et al. (2014) showed with simulations that a poleward wind shift near Antarctic Peninsula can produce an intense warming of subsurface coastal waters that exceeds 2°C at 200–700 m depth. This confined heat could affect sea ice extent if it is

* Corresponding author, E-mail: fuflima@gmail.com

brought up by enhanced Ekman pumping. Some numeric simulations suggest that drastic changes in winter Antarctic sea ice extent generate significant impacts on the Southern Hemisphere climate. For instance, Mitchell and Hills (1986) observed that when removing all existing sea ice below 66°S, there is a large increase in the sensible heat flux at low levels of the atmosphere in these regions. This heat confined above Antarctica implies in a reduction of about 2 $m \cdot s^{-1}$ of the westerly flow along the new sea ice margin.

The most important role of the sea ice in the climate system is related to the reflection of incident solar radiation. Moreover, sea ice is an efficient isolator, which limits momentum, heat and mass exchanges between the atmosphere and adjacent ocean (Parkinson, 2004). Furthermore, sea ice plays an important role in upper ocean temperature and salinity changes and, therefore, in adjacent water density and the formation of intermediate and bottom ocean waters (Brown et al., 2001). The Antarctic sea ice is characterized by a pronounced seasonal cycle (Thomas and Dieckmann, 2003), even though trends are observed in some seasons (Zwally et al., 2002). Although some studies have examined the role of the oceans in the Antarctic sea ice variability, many scientific questions remain to be investigated to understand atmosphere-ocean-sea-ice coupling mechanisms on various time-scales. To illustrate the importance of these issues, Gordon (1981) estimated that the heat stored below the ocean's pycnocline is responsible for 50% of the necessary heat for spring sea ice melting. Therefore, mechanisms inducing upwelling could also enhance melting at the sea ice margins.

Observational studies focusing on sea ice and atmosphere interactions have shown strong coupling on a broad range of scales (Lima and Carvalho, 2008; Wendler and Nagashima, 1987; Walsh, 1983). Lima and Carvalho (2008) showed that intraseasonal anomalies in atmospheric circulation were related to extreme variability in sea ice area observed also on intraseasonal time-scales. These events were associated with midlatitude wave trains propagating from the tropics to the extratropics (Mo and Paegle, 2001; Lau et al., 1994; Ghil and Mo, 1991). Hall and Visbeck (2002) suggested that the Antarctic Oscillation (Gong and Wang, 1999) may cause significant impacts on sea ice due to mass exchanges between Polar Regions and the extratropics and impacts on Ekman layer dynamics on intraseasonal time-scales.

Furthermore, atmospheric teleconnection mechanisms generated by tropical phenomena on intraseasonal time-scales, such as the Madden-Julian Oscillation (MJO) (Madden and Julian, 1994) affect global circulation and cause impacts on the Antarctic sea ice (Jin et al., 2013; Jia et al., 2011; Jones et al., 2011; Carvalho et al., 2005; Zhang, 2005). Carleton (2003) suggests that convective anomalies propagating longitudinally induce a Rossby-wave train pattern known as Pacific South American (PSA), which affects the extratropical Pacific. Lima and Carvalho (2008) related the PSA to variations in sea ice area on intraseasonal time-scales on the Weddell, Amundsen and Bellingshausen seas. They identified that extreme contraction (expansion) anomalies of sea ice area on intraseasonal time-scale are associated with opposite phases of the PSA and are related to warm (cold) temperature advection at low levels and warm (cold) sea surface temperature anomalies. Interactions that occur in the Southern Ocean between the atmosphere, ocean, and cryosphere greatly influence the dynamics of the entire climate system through the formation of water masses and the sequestration of heat, freshwater, carbon, and other properties (Weijer et al., 2012; Rintoul et al., 2001). The Weddell and Ross oceanic basins are considered key regions for the formation of bottom waters masses (Thoma et al., 2006; Gordon et al., 2001; Comiso and Gordon, 1998; Markus et al., 1998; Martinson and Iannuzzi, 1998; Jacobs et al., 1970), and trends in sea ice extent on the Weddell and Ross seas could directly affect oceanic circulations. More (less) ice production in these seas could strengthen (weaken) deep flow of Atlantic and Pacific Meridional Overturning Circulation by changing surface temperature and density (which affect local oceanic stratification) (Tomczak and Godfrey, 2003). Therefore, the present study focuses on the Weddell Sea, given its importance for the global oceanic circulation.

The main objective of this study is to examine mechanisms associating ocean-atmospheric interactions with sea ice variability on intraseasonal time-scales. More specifically, this study examines the response of the Southern Hemisphere Ocean (Southern Ocean for simplification) to the propagation of atmospheric waves on intraseasonal time-scales and the role of these interactions in the Weddell sea ice variability.

2 Data

Daily sea ice extent (SIE) in the Weddell Sea (Figure 1) is estimated from the Scanning Multichannel Microwave Radiometer (SMMR) and Special Sensor Microwave/ Imager (Nimbus-7 SMMR; DMSP-F8, F11, and F13 SSM/I) at a grid cell size of 25 × 25 km^2, available from the US National Snow and Ice Data Center (NSIDC; Stroeve 2003). The ice-extent indicates whether ice is present; here, ice is considered to exist in a pixel if the sea ice concentration exceeds 15 percent. The SIE data originally begin in October 1978; however, data before 1989 was not included because of gaps and availability every 2 d. The SIE data investigated here are daily estimates and cover the 1989–2013 period.

The atmospheric dynamics is characterized with the National Centers for Environmental Prediction (NCEP) Climate Forecast System Reanalysis (CFSR; Saha et al., 2010) at 1° latitude/longitude grid spacing from 1 January 1989 to 31 December 2013. The following variables are examined: daily averages of the zonal and meridional

Figure 1 Map of Antarctica and surrounding seas (60°S–90°S) in stereographic polar perspective (obtained from Turner and Pendlebury, 2004). Weddell Sea is highlighted by the ellipse in red.

components of the winds at 10 meters (U10 and V10, respectively). The advantages of CFSR relative to the previous NCEP reanalysis include high horizontal and vertical resolutions, improvements in data assimilation, and first-guess fields originated from a coupled atmosphere–land–ocean–ice system (Higgins et al., 2010; Saha et al., 2010).

Daily average zonal and meridional components of wind stress at 10 m (τ_x e τ_y, respectively) were calculated using the bulk formula (Eq. 1), where u is the wind velocity, ρ_{air} is the air density (considered here as 1.2 kg·m^{-3}) and C_D is the drag coefficient for the ocean (considered here as 1.2×10^{-3}). More details about bulk formula, wind stress and the drag coefficient for the ocean can be seen in Large and Pond (1981), Yelland and Taylor (1996) and Kara et al. (2006).

$$\boldsymbol{\tau}=\rho_{air}C_D\boldsymbol{u}|u| \quad (1)$$

The case studies that represent the most negative and positive sea ice extreme intraseasonal anomaly events, respectively, are chosen using 5-d average (pentad) data of surface ocean currents from National Oceanic and Atmospheric Administration (NOAA)/Ocean Surface Currents Analyses–Real Time (OSCAR). The OSCAR product is a direct computation of global surface currents using satellite sea surface height, wind, and sea surface temperature. Currents are calculated using a quasi-steady geostrophic model along with an eddy viscosity based wind-driven ageostrophic component and a thermal wind adjustment. The model calculates a surface current averaged over the top 30 m of the upper ocean (Bonjean and Lagerloef, 2002). Data used in this study are spatially filtered to 1 degree grid space resolution and was obtained from Earth Space Research (ESR) (https://www.esr.org/).

Daily high resolution data estimated from radiometers and in situ observations of sea surface temperature (SST) and sea ice fraction (http://mur.jpl.nasa.gov) are also used to correlate ocean currents to surface warm or cold anomalies. SST data are produced by the Group for High Resolution Sea Surface Temperature (GHRSST) as a retrospective dataset (four day latency) and near-real-time dataset (one day latency) using wavelet basis functions in an optimal interpolation approach on a global 0.01 degree grid (Chin et al., 2014, 2010, 1998; Vazquez-Cuervo et al., 2013; Armstrong at al., 2012; Dash et al., 2012; Haines et al., 2007; Mariano and Brown, 1992; Mariano, 1990). The ice concentration data are from the archives at the EUMETSAT Ocean and Sea Ice Satellite Application Facility (OSI SAF) High Latitude Processing Center and are also used for an improved SST parameterization for the high-latitudes. All this data were examined here in the Southern Ocean, for all longitudes and latitudes from 40°S to 90°S.

Wind stress τ affects the oceanic Ekman layer (approximately between 0 to 100 m) by transferring momentum by friction. The balance of forces in the Ekman layer is obtained between friction, pressure gradient force and Coriolis force (Cushman-Roisin and Deleersnijder, 2005; Tomczak and Godfrey, 2003). However, describing the dynamics of the Ekman layer is a complex problem that often requires turbulent mixing coefficients that are difficult to determine. One alternative approach to investigate the Ekman layer dynamics is by evaluating mass transport. The component of water transport layer induced by the wind is perpendicular to the average direction of the wind (and τ), whereas the Coriolis force deflects the Ekman transport to left in the SH and to right in the NH. Considering the balance of forces in the Ekman layer, we can derive Eqs. 2 and 3, where ρ_0 is sea water density (considered here as 1025 kg·m^{-3}), f is the Coriolis parameter, U_e and V_e are zonal and meridional components of Ekman mass transport, respectively, u and v are zonal and meridional components of Ekman's velocity and z_e is the base of the Ekman layer (considered here as the depth of 100 m). Descriptions of zonal and meridional Ekman layer mass transport for global ocean and for individual oceanic basins can be seen in Levitus (1987). Applications of Eqs. 2 and 3 can be seen in Chereskin and Roemmich (1991).

$$U_e=\frac{\tau_y}{\rho_0 f}=\int_{z_e}^{0}u\mathrm{d}z \quad (2)$$

$$V_e=-\frac{\tau_x}{\rho_0 f}=\int_{z_e}^{0}v\mathrm{d}z \quad (3)$$

The resulting convergence and divergence of water masses due to Ekman transport is known as the Ekman pumping. Using the continuity equation (Eq. 4), it is possible to calculate the vertical movement of water in the oceanic Ekman layer (w_e) resulting from the average Ekman mass transport (Eqs. 5 and 6), where:

$$\frac{\partial u}{\partial x}+\frac{\partial v}{\partial y}+\frac{\partial w}{\partial z}=0 \tag{4}$$

$$-\int_{z_e}^{0}\frac{\partial w}{\partial z}\mathrm{d}z=\frac{\partial U_e}{\partial x}+\frac{\partial V_e}{\partial y} \tag{5}$$

$$w_e=\frac{\partial U_e}{\partial x}+\frac{\partial V_e}{\partial y} \tag{6}$$

By rewriting the terms of the Ekman transport as a function of τ, we obtain the relationship between Ekman pumping w_e and the rotational of wind stress, where positive (negative) rotational of τ is associated with divergence (convergence) in oceanic Ekman layer and upward (downward) movement or upwelling (downwelling) due to Ekman pumping (Tomczak and Godfrey, 2003; Large and Pond, 1981).

3 Results

The relative importance of intraseasonal variability in SIE was demonstrated by performing spectral analysis. The spectrum of the Weddell SIE variability was obtained based on the Fourier Transform. First and foremost, long-term trends and the annual cycle of the time series were removed. The spectral analysis was performed for the winter period (June, July and August–JJA). The spectrum was obtained as an ensemble of the spectra of the 25 winters (1989–2013). This study focuses on the Austral winter (JJA) because previous studies indicated that links between atmospheric perturbations and SIE on intraseasonal time-scales (20–100 d) are stronger during this season (Lima and Carvalho, 2008). The ensemble winter spectrum of the Weddell SIE shows peaks above the 95% confidence level on intraseasonal time-scales approximately between 10 to 60 d (Figure 2). The 95% confidence level was calculated based on red noise values multiplied by the value obtained from a Qui-Square table (according to the number of degree of freedom) and normalized by the number of degree of freedom.

Based on these results, the Weddell SIE data were bandpass-filtered to retain anomalies between 20–100 d. A Fast Fourier transform (FFT) filter was used for this purpose (e.g. Helms, 1967). The relatively wide 20–100 d band was chosen to avoid including synoptic-scale variance (i.e, highest frequency retained should be less than 1/20 d) and to account for the fast decrease of the response function (from 1 to 0.5) of the filter near the border of the band (not shown).

Extreme intraseasonal SIE anomalies were then defined based on the quartiles of the distribution of anomalies following Lima and Carvalho (2008). Extreme positive intraseasonal sea ice anomalies related to expansion (negative related to contraction) are defined here when the SIE intraseasonal anomalies are greater or equal than the upper quartile (less or equal the lower quartile) of the distribution of anomalies observed during JJA. Independent extreme events were separated according to "persistence". Persistence was defined as the number of consecutive days that satisfied the threshold conditions discussed above. Figure 3 shows the distribution of persistence (in days) of extreme intraseasonal SIE contraction and expansion events from 1989–2013. For the sake of simplification, extreme intraseasonal SIE contraction (expansion) will be referred to as $SIEC_{IS}$ ($SIEE_{IS}$). During the period of study we found 42 (51) $SIEC_{IS}$ ($SIEE_{IS}$) events. The most persistent $SIEC_{IS}$ ($SIEE_{IS}$) event lasted about 35 (38) d. Figure 3 also shows that the distribution of intraseasonal $SIEE_{IS}$ anomalies is displaced toward more persistent events compared to $SIEC_{IS}$. The average and standard deviation of the duration of $SIEC_{IS}$ ($SIEE_{IS}$) is 14.0 ± 7.7 (17.5 ± 9.4) d.

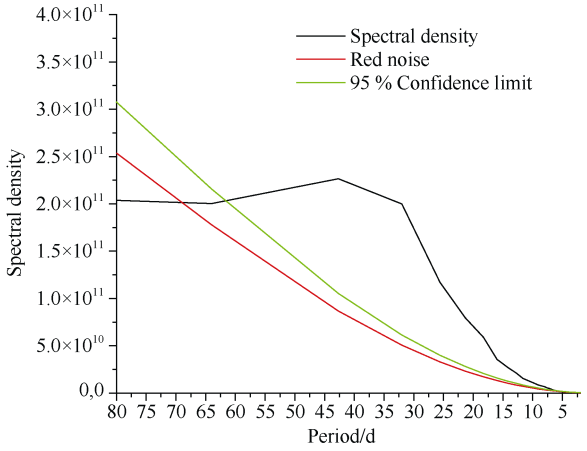

Figure 2 Winter ensemble spectral density of Weddell SIE total anomalies (annual cycle removed) during 1989–2013 (black line). Red (green) solid line represents the background red noise (95% confidence limit) spectrum. Daniell window (L = 3) was applied to the spectrum.

Variations in the Ekman dynamics on intraseasonal time-scales associated with extreme SIE_{IS} are examined with lag composites of zonal and meridional Ekman mass transport and Ekman pumping anomalies. The objective of the lag composites is to show how extratropical wave trains propagating in the atmosphere force the upper ocean on intraseasonal time-scales and how these changes can be conducive to extreme $SIEC_{IS}$ and $SIEE_{IS}$ anomalies. Lag-0 corresponds to the date when sea ice anomalies were classified as $SIEC_{IS}$ and $SIEE_{IS}$ (Figures 4–9). Negative (positive) lags indicate that the observed patterns lead (lag) the events by the number of days indicated at the top of each figure. All variables analyzed in these composites were bandpass-filtered (20–100 d band was retained). The statistical significance of the anomalies was assessed using a *t*-Student test at 5% level. The degrees of freedom were estimated considering all independent events with persistence $\geqslant$ 2 d.

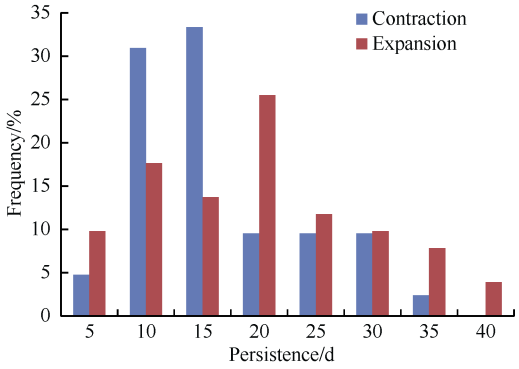

Figure 3 Persistence (unit: d) of extreme negative (contraction) and positive (expansion) sea ice anomalies

Figures 4 and 5 show lag composites of intraseasonal anomalies of the zonal Ekman mass transport (U_{IS}). Lag composites are shown poleward of 1° because of the Coriolis parameter *f*. Focusing on the Weddell Sea (centered approximately at 45°W), we observe during $SIEC_{IS}$ (Figure 4) positive U_{IS} anomalies (westerly anomalies) east of the Weddell sea ice edges and negative anomalies (easterly anomalies), west of the Antarctica Peninsula leading the events (negative lags). This configuration persists and propagates eastward between *lag* = −15 d (not shown) and *lag* = 0. The combination of positive U_{IS} anomalies associated with the wave train and the Antarctica Peninsula acting as a barrier characterize the zonal divergence of the Ekman layer water mass. After *lag* = 0, we observe an opposite phase of the wave train acting on the same region leading to a pattern of anomalies that favors convergence of U_{IS} in the vicinity of Weddell Sea for positive lags.

The main difference between extreme $SIEC_{IS}$ and $SIEE_{IS}$ events (Figures 4 and 5) is that these events are characterized by opposite phases of the wave train as indicated by the opposite sign of the anomalies at all lags.

Figures 6 and 7 complements the previous analysis by showing lag composites of intraseasonal anomalies of meridional Ekman mass transport (V_{IS}) associated with extreme $SIEC_{IS}$ and $SIEE_{IS}$ events (Figures 6 and 7, respectively). Positive anomalies are observed north and negative south of the Weddell Sea leading the event (*lag* = −8 d) and during the event (*lag* = 0). Consistent with the propagating characteristic of the phenomenon, opposite pattern of V_{IS} is observed a few days after the event. The configuration of the anomalies indicates meridional divergence of the Ekman layer mass transport leading the $SIEC_{IS}$ events. Conversely, V_{IS} anomalies observed during extreme $SIEE_{IS}$ events indicate that these events are associated with the opposite phase of the wave train acting on the Weddell Sea, as it propagates from tropical to extratropical Pacific. This phase favors convergence of Ekman mass transport leading these events.

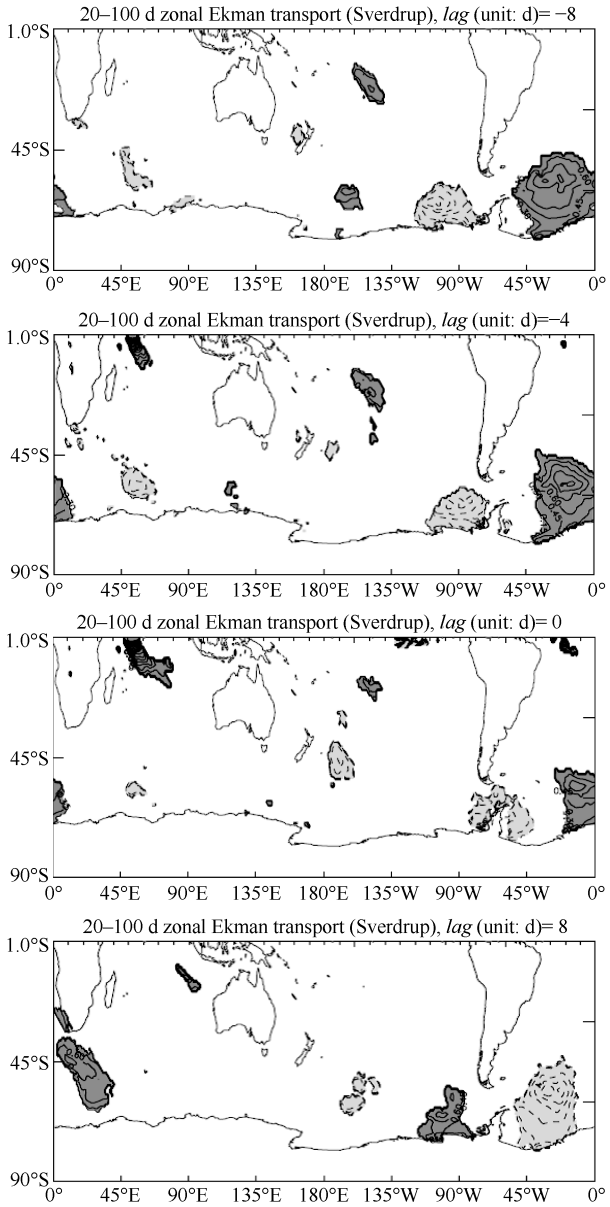

Figure 4 Lag composites of intraseasonal anomaly of zonal Ekman mass transport (U_{IS}) during periods of winter extreme intraseasonal Weddell sea ice extent (SIE) associated with sea ice contraction ($SIEC_{IS}$). Solid (dashed) lines indicate positive (negative) values. First contour 0.15 Sv (−4.5 Sv) with an interval of 0.15 Sv to U_{IS}. Shades show statistically significant anomalies at 5% significance based on *t*-Student test. Lags are indicated at the top of the figure. *Lag* = −8 (−4) d represents 8 (4) d prior the event, *lag* = 0 is the day of the event and *lag* = 8 is 8 d after the event.

All lag composites seem to indicate that anomalies are stronger, more spatially coherent and consistent from event-to-event for negative lags, that is, prior to the occurrence of SIE (Figures 4–7). Finally, lag composites of intraseasonal Ekman pumping anomalies (w_{IS}) associated with extreme SIE events are shown in Figures 8 and 9.

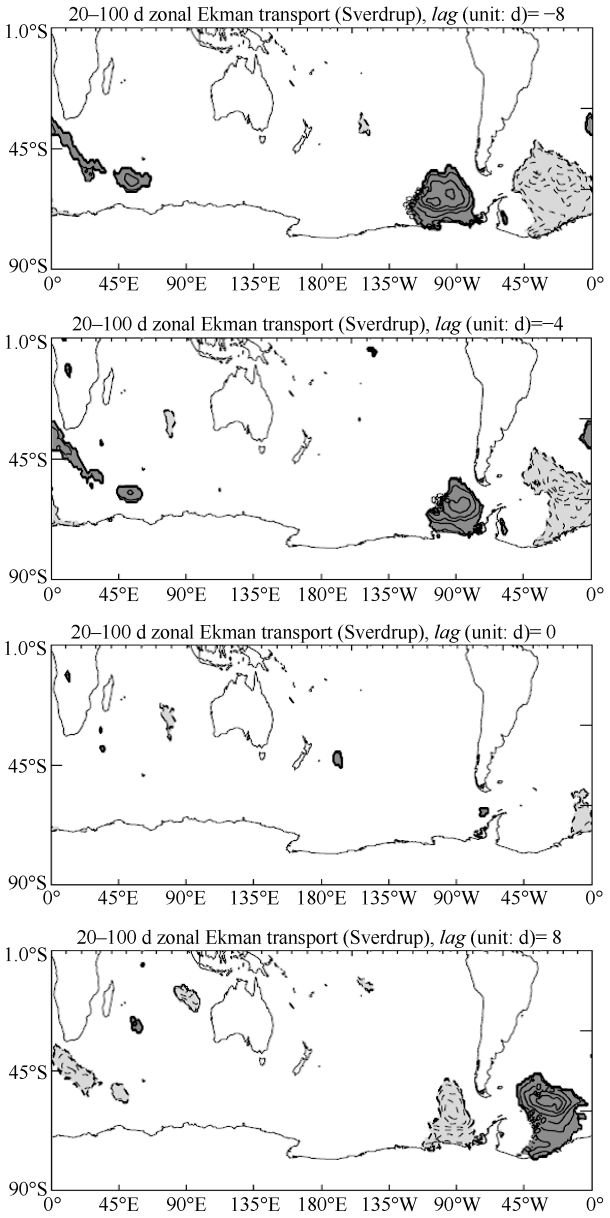

Figure 5 Lag composites of intraseasonal anomaly of zonal Ekman mass transport (U_{IS}) during periods of winter extreme intraseasonal Weddell sea ice extent (SIE**)** associated with sea ice expantion ($SIEE_{IS}$**)**. Solid (dashed) lines indicate positive (negative) values. First contour 0.15 Sv (−4.5 Sv) with an interval of 0.15 Sv to U_{IS}. Shades show statistically significant anomalies at 5% significance based on *t*-Student test. Lags are indicated at the top of the figure. *Lag* = −8 (−4) d represents 8 (4) d prior the event, *lag* = 0 is the day of the event and *lag* = 8 is 8 d after the event.

Lag composites of U_{IS} and V_{IS} examined in our previous analyses (Figures 4–6 and 7) indicated that Ekman mass divergence is observed in the vicinity of Weddell Sea prior to the occurrence of extreme $SIEC_{IS}$ (negative lags). Figure 8 suggests that the divergence is related to positive Ekman pumping or upwelling all over the Weddell Sea.

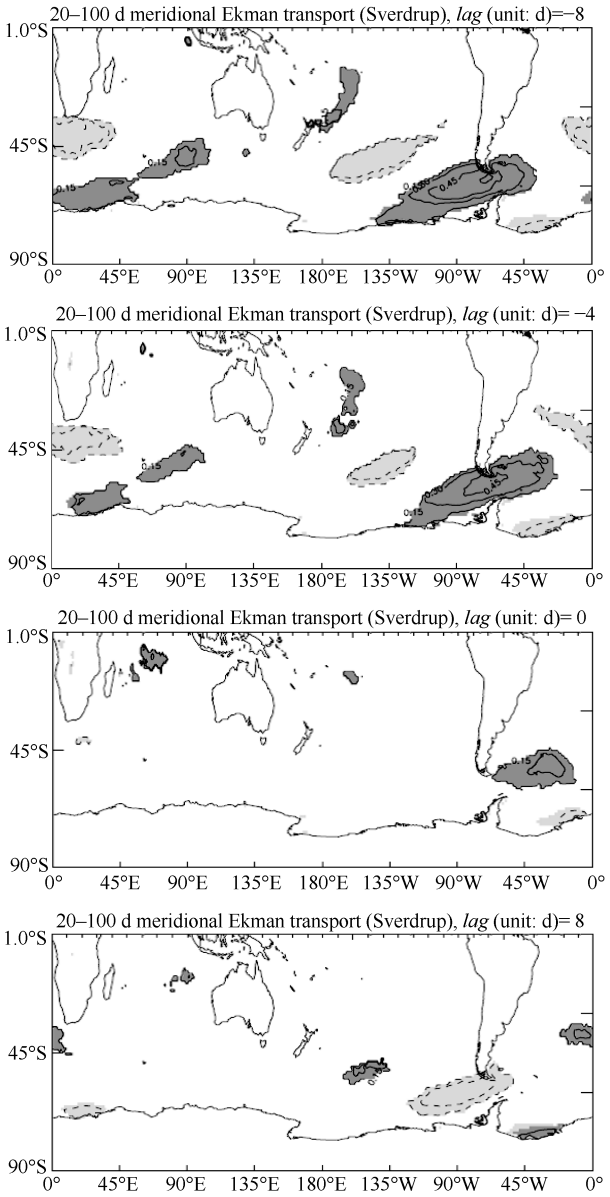

Figure 6 Same as Figure 4, but for intraseasonal anomalies of meridional Ekman mass transport (V_{IS}). Solid (dashed) lines indicate positive (negative) values. First contour: 0.15 Sv (−4.5 Sv) with an interval of 0.15 Sv to V_{IS}. Lags (unit: d) are indicated at the top of the figures.

According to Gordon (1981), sea-air heat exchange between latitudes of 60°S and 70°S in ice-free regions corresponds to 50% of the total heat necessary to melt winter sea ice during the austral spring. The remaining heat necessary to melt sea ice is supplied by the oceanic heat stored below the pycnocline of the Southern Ocean. This heat is transferred to sea surface by the Ekman pumping. Thus, we suggest that relatively warmer waters in oceanic sub-surface layers are pumped into shallower waters near the Weddell sea ice margins induced by the propagation of wave trains, contributing to sea ice contraction. Conversely, extreme

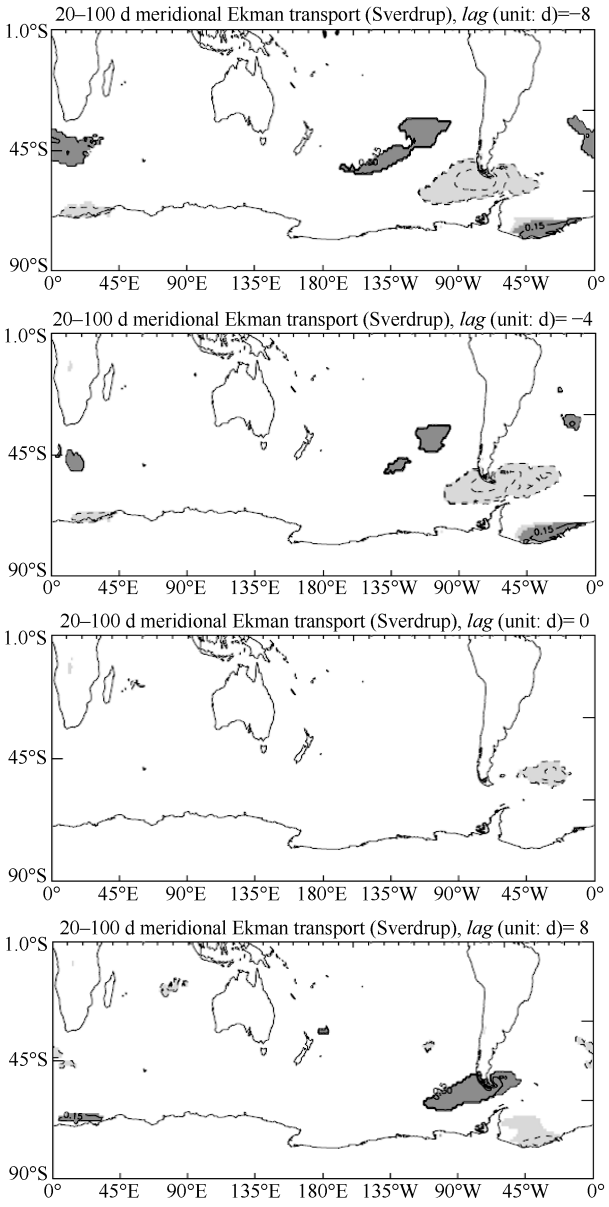

Figure 7 Same as Figure 5, but for intraseasonal anomalies of meridional Ekman mass transport (V_{IS}). Solid (dashed) lines indicate positive (negative) values. First contour: 0.15 Sv (−4.5 Sv) with an interval of 0.15 Sv to V_{IS}. Lags (unit: d) are indicated at the top of the figures.

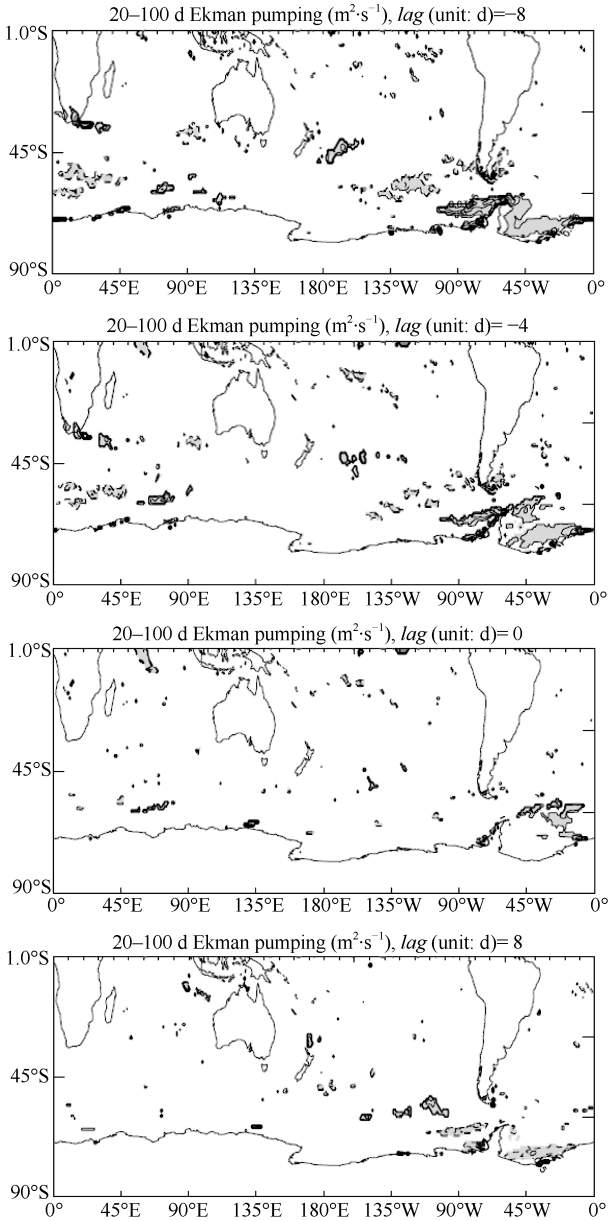

Figure 8 Same as Figure 6, but for intraseasonal anomalies of Ekman pumping (w_{IS}). Solid (dashed) lines indicate positive (negative) anomalies starting at 0.015 $m^2 \cdot s^{-1}$ (−0,09 $m^2 \cdot s^{-1}$) with 0.015 $m^2 \cdot s^{-1}$ interval. In the composities, *lag* = −8 (−4) d represents 8 (4) d before the event, *lag* = 0 represents the day along with the event and *lag* = 8 d represents 8 d after the event.

$SIEE_{IS}$ are associated with Ekman mass convergence and negative Ekman pumping or downwelling all over the Weddell Sea (Figure 9). The hypothesized coupled mechanism is that extreme $SIEE_{IS}$ events are associated with more saline and denser surface waters (due to less sea ice melting), that generate downwelling in the vicinity of the Weddell Sea.

Figure 10 summarizes the mechanisms describing the Ekman dynamics on intraseasonal time-scales related to extreme Weddell SIE. In this figure, τ_{ISx} and τ_{ISy} represent zonal and meridional wind stress, respectively.

Figure 10a (10b) schematically illustrates the conditions leading to $SIEC_{IS}$ ($SIEE_{IS}$) and shows how wind stress, caused by intraseasonal anomalies associated with extratropical wave trains, induces upwelling (downwelling) that contributes to the observed anomalies in sea ice. In sea ice covered regions, the winds exert stress on sea ice first and then sea ice movement exerts stress on the ocean surface.

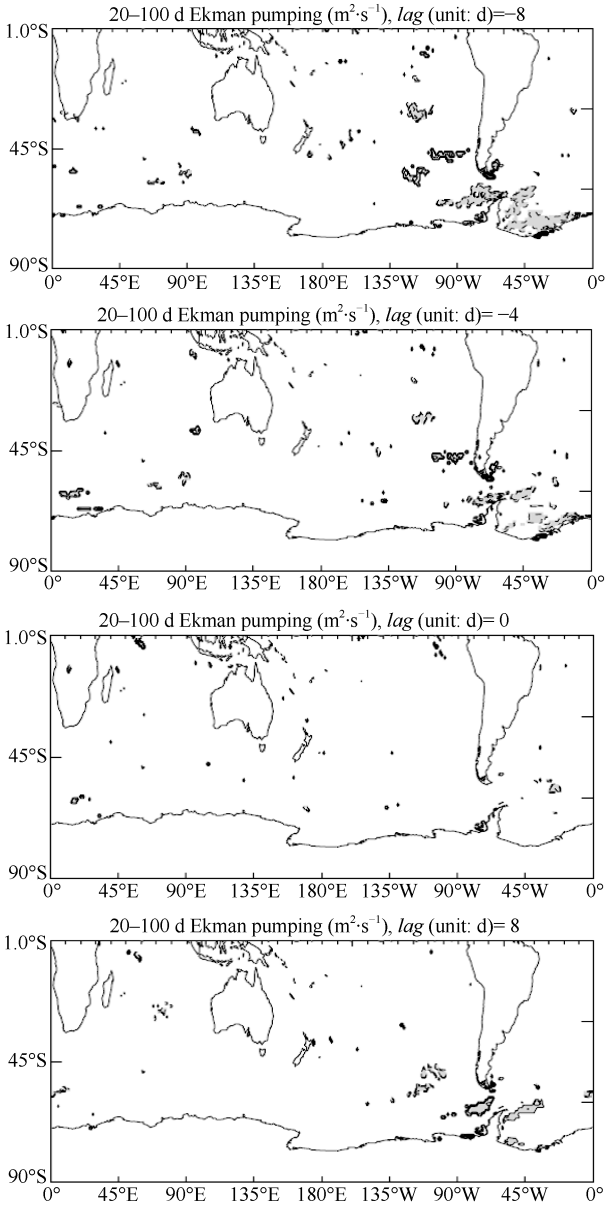

Figure 9 Same as Figure 7, but for intraseasonal anomalies of Ekman pumping (w_{IS}). Solid (dashed) lines indicate positive (negative) anomalies starting at 0.015 $m^2 \cdot s^{-1}$ (−0.09 $m^2 \cdot s^{-1}$) with 0.015 $m^2 \cdot s^{-1}$ interval. In the composities, *lag* = −8 (−4) d represents 8 (4) d before the event, *lag* = 0 represents the day along with the event and *lag* = 8 d represents 8 d after the event.

4 Case study: persistent extreme $SIEC_{IS}$ and $SIEE_{IS}$ events

This section examines individual cases of extreme Weddell SIE_{IS} events with the objective of investigating in detail patterns of anomalies obtained in lag composites previously discussed. The focus of this analysis is on the magnitude of these variations and spatial extent of the Weddell sea ice concentration. Additionally, this section compares results obtained from two independent data sets (reanalysis used in lag composites, and satellite and in situ data investigated in the case-studies). Cases were selected based on the persistence of the intraseasonal anomalies of expansion and contraction as discussed before. We investigated the two most persistent $SIEC_{IS}$ and $SIEE_{IS}$ events, which lasted approximately 35 and 38 d (*super-cases*), respectively. The most persistent $SIEC_{IS}$ event started on July 5, 2006; while the most persistent $SIEE_{IS}$ event started on August 15, 2010. The beginning of the event refers to the date when intraseasonal anomalies of sea ice extent exceeded (were below) the 75th (25th) percentile of the anomalies, as discussed in section 3.

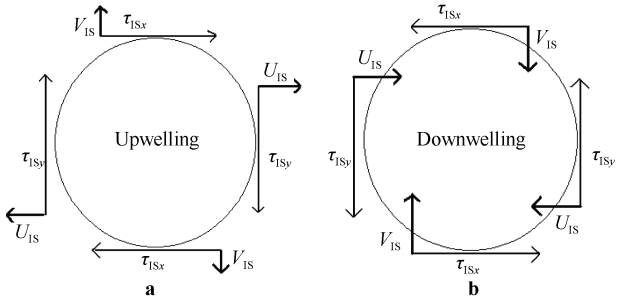

Figure 10 Representation of τ_{ISx}, τ_{ISy}, U_{IS} e V_{IS} vectors and relationships with upwelling in Ekman layer associated with extreme $SIEC_{IS}$ (**a**) and downwelling in Ekman layer associated with extreme $SIEE_{IS}$ (**b**).

Figure 11 shows the evolution of intraseasonal anomalies of surface ocean currents (vectors) and Antarctic sea ice concentration (colors) during the $SIEC_{IS}$ *super-case*. The eastward propagation of sea ice anomalies is evident in the lag-composites (from 11a to 11h). For instance, from *lag* = −5 pentads to *lag* = −2 pentads the anomalies of sea ice concentration change from less than −20% to +20% at the margin of the Weddell sea ice. This represents a variation of more than 40% of the sea ice concentration in a period of about 15 d. Notice that west of the Antarctica Peninsula anomalies also change from positive to negative during the same period and with variations exhibiting similar magnitude. Between *lag* = −1 pentad and *lag* = 0, positive anomalies propagate eastward and are progressively replaced by negative anomalies. Over time, negative anomalies in sea ice concentration (−20%) dominate the Weddell winter sea ice edges in positive *lags* (*lags*=1 to 2 pentads). The propagation of the anomalies is consistent with the circumpolar propagation of wave train on intraseasonal time-scales. Additionally, surface ocean currents seem to intensify next to negative sea ice concentration anomalies at the Weddell sea ice margin and western Antarctica Peninsula during *lag*=−1 and *lag*=0. This intensification could be associated with the intensification of heat advection and Ekman layer divergence and upwelling.

Figure 12 shows the temporal evolution of intraseasonal anomalies of Antarctic sea ice concentration related to the *super-case* $SIEE_{IS}$. Similarly, this event shows a gradual change in sea ice concentration anomalies at the margin of the Weddell Sea and western Antarctica associated with the circumpolar propagation of atmospheric wave train (from 12a to 12h). Anomalies change from predominantly negative (>−20% in concentration) to positive (>20% in concentration) from *lag*=−5 pentads to *lag*=−1. A complete reverse in the anomalies is observed approximately from *lag*=0 pentad to *lag*=2 pentads. In general, we observed divergence (convergence) of surface ocean currents associated with $SIEC_{IS}$ ($SIEE_{IS}$) anomalies. We also observed that surface ocean currents are less intense during $SIEE_{IS}$ compared to the $SIEC_{IS}$ event. We recall that this discussion focuses only on anomalies at the margin of the Weddell Sea.

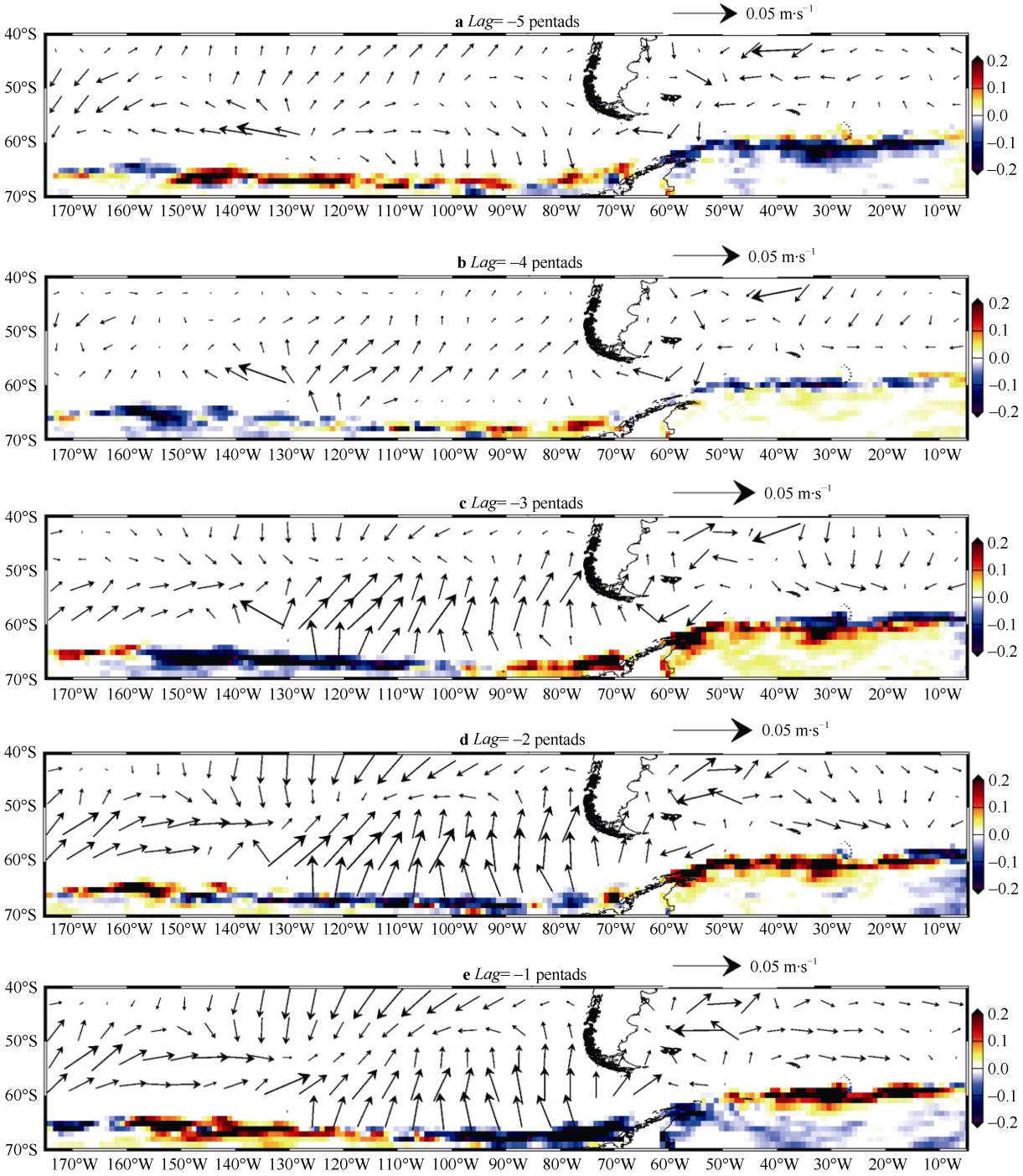

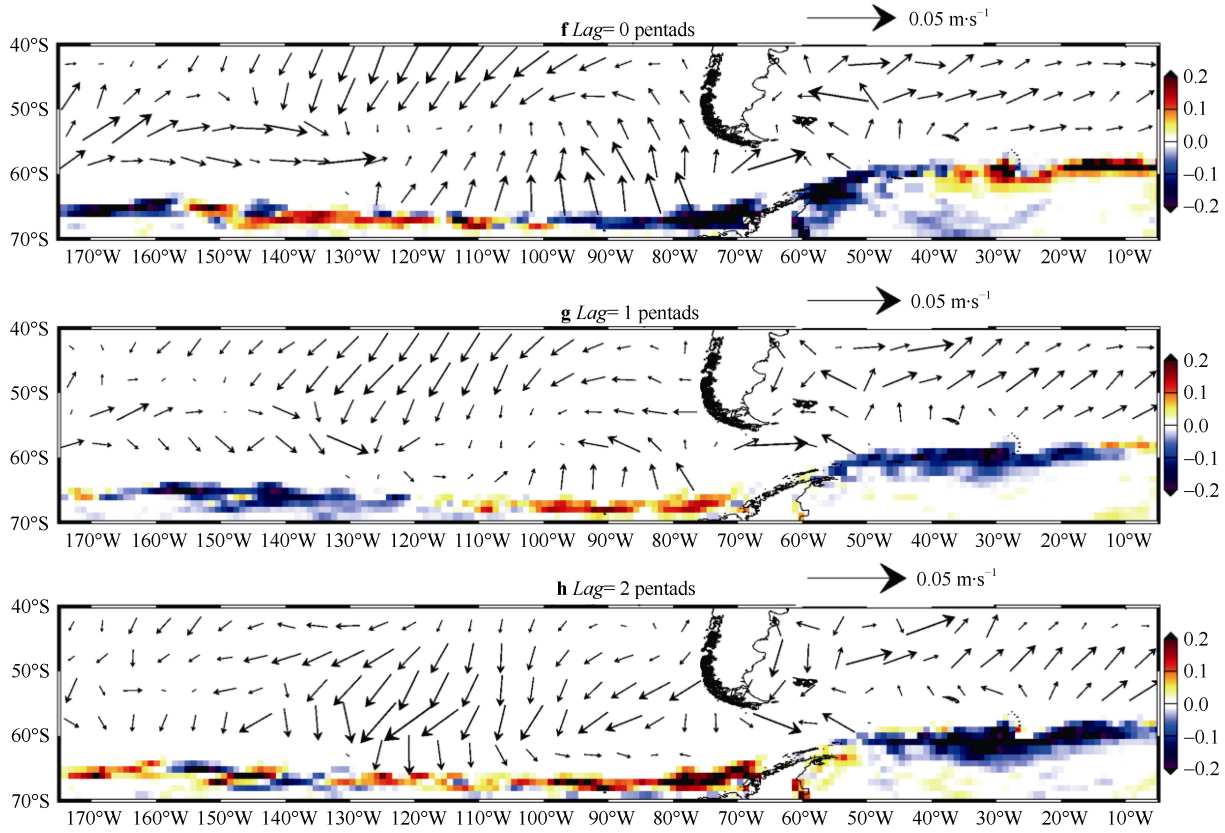

Figure 11 Intraseasonal anomalies of Antarctic sea ice concentration (in color) and surface ocean currents (vectors) associated with the most persistent event of extreme Weddell sea ice extent contraction ($SIEC_{IS}$) on intraseasonal time-scales for 5 (**a**), 4 (**b**), 3 (**c**), 2 (**d**) and 1 (**e**) pentad(s) before the $SIEC_{IS}$, during the first pentad of the occurrence of extreme $SIEC_{IS}$ (**f**), and 1 (**g**) and 2 (**h**) pentad(s) after the $SIEC_{IS}$. The range of the anomalies (in colors) is given by a factor divided by 100. Only the vectors above 0.01 $m \cdot s^{-1}$ were displayed.

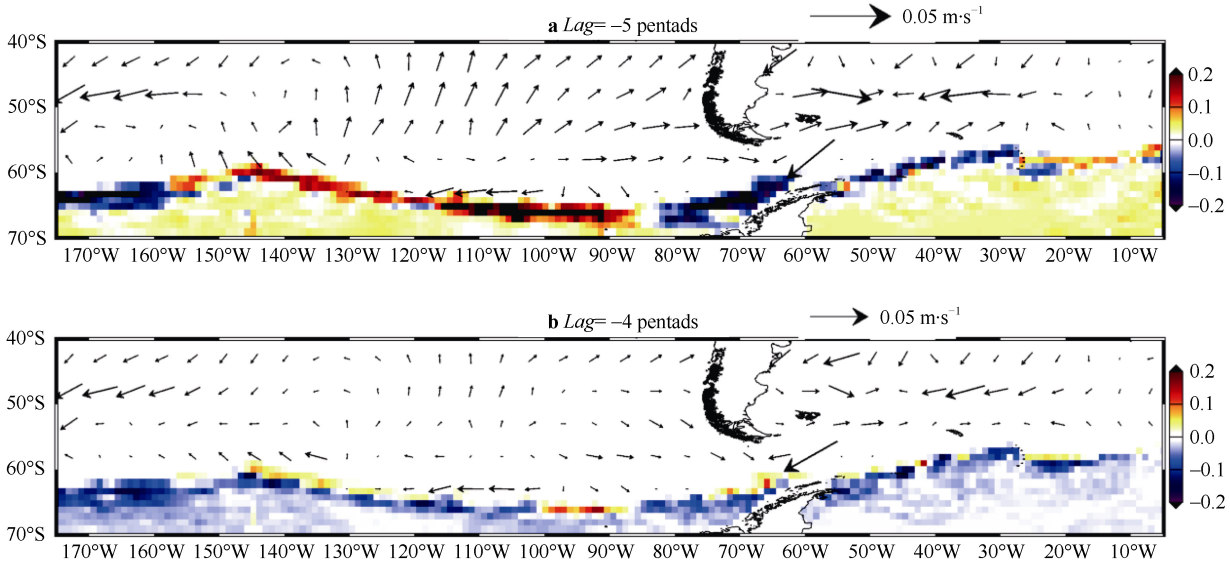

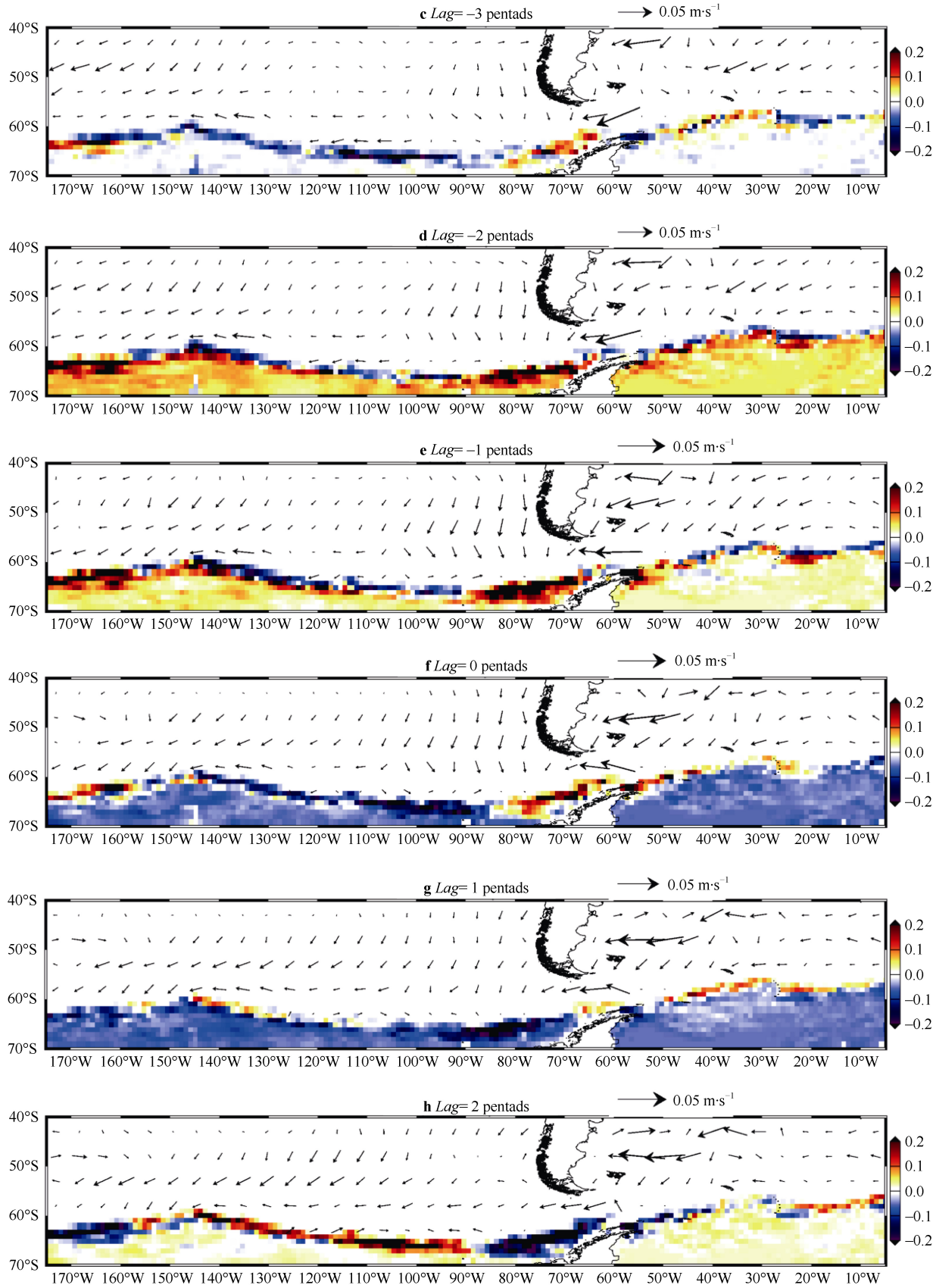

Figure 12 Same as Figure 11, but for the most persistent event of intraseasonal extreme sea ice extent expansion ($SIEE_{IS}$) in the Weddell Sea.

5 Conclusions

This study aimed to explore mechanisms associated with extreme intraseasonal Antarctic sea ice extent focusing on the ocean's response to atmospheric forcing on intraseasonal time-scales. Previous studies have shown that perturbations in the surface wind caused by atmospheric wave trains on intraseasonal time-scales propagating toward high-latitudes of the Southern Hemisphere can cause oscillations in sea ice extent on similar time-scales (e.g., Lima and Carvalho, 2008). The present study specifically investigates resulting interactions between wind stress and ocean currents associated with intraseasonal wave trains and implications for the meridional Ekman transport. The winter average spectrum of Weddell SIE (obtained between 1989 and 2013) clearly revealed the relative importance of sea ice fluctuations on intraseasonal time-scales. Lag-composites of zonal and meridional Ekman transport, which are perpendicular and to the left of the wind stress in the SH, show that mass divergence in the Ekman layer north of the Weddell Sea and Antarctica Peninsula occur prior to the observation of extreme $SIEC_{IS}$ (negative lags), while mass convergence is observed prior to extreme $SIEE_{IS}$. Consistent with divergence (convergence) of mass in the Ekman layer, we observed intraseasonal anomalies of Ekman pumping related to upwelling (downwelling) prior to the occurrence of extreme $SIEC_{IS}$ ($SIEE_{IS}$). Gordon (1981) showed that intermediate Antarctic waters, which are warmer in winter compared to surface waters, are directed toward the ocean surface by Ekman pumping, causing the Austral spring sea ice to melt. Our study suggested that coupling mechanisms inducing intraseasonal variability in sea ice margins can be largely explained by the Ekman pumping: warmer intermediate waters enhance sea ice melting ($SIEC_{IS}$) whereas water mass convergence induces the expansion of the sea ice ($SIEE_{IS}$) probably due to wind-driven sea ice advection.

Case studies were examined in details to verify mechanisms and better understand the magnitude of variations in sea ice concentration (%) associated with persistent $SIEC_{IS}$ and $SIEE_{IS}$ events. This analysis was carried out by examining the two most persistent events during 1989–2013. Coupled mechanisms proposed to explain variations in sea ice extent based on lag-composites were reproduced in the case-study. Crucially, we observed variations of 40% in sea ice concentration at the margin of the Weddell and western Antarctica Peninsula sea ice within a period as short as 2–4 pentads. These fast changes in sea ice concentration are associated with the eastward propagation of wave train on intraseasonal time-scales. This study also suggested that surface ocean currents intensify next to the coastal regions during extreme $SIEC_{IS}$ event. This intensification could be associated with heat advection or intensified Ekman layer divergence and upwelling. Conversely, Spencer et al. (2014) showed that the warming of subsurface waters is associated with weak near-shore Ekman pumping and weak coastal currents; our results suggest that this mechanism is likely related to $SIEE_{IS}$ events. Although this study focused on the Weddell sea ice, mechanisms coupling atmospheric midlatitude wave trains to variations in sea ice investigated here could be important for all circumpolar seas and could be relevant at other temporal scales.

The Antarctica Peninsula has been experiencing one of the largest rates of warming in high latitudes of the Southern Hemisphere (Vaughan et al., 2003; Smith and Stammerjohn, 2001). The collapse of immense sea ice-shelves in the vicinity of Weddell Sea like Larsen A, Larsen B ice-shelf and the north part of Larsen C in recent (Glasser and Scambos, 2008; Rignot et al., 2004; Scambos et al., 2004; Vaughan and Doake, 1996) have demonstrated how fast and unpredictable the cryosphere changes in a warming planet (Vaughan et al., 2003). Understanding mechanisms associated with the coupling between atmospheric circulation and ocean currents and implications for sea ice patterns on multiple time-scales is crucial to evaluate the evolution of the cryosphere and to realistically assess future projections of climate change.

Acknowledgments The CFSR data used in this research were developed by NOAA's National Centers for Environmental Prediction (NCEP) and provided by NCAR. We thank the NSIDC for making sea ice extent data available; NASA/JPL for sea ice fraction; and ESR for ocean currents. We thank Dr. Charles Jones for computational support. We thank the anonymous reviewers for their thoughtful comments and suggestions. This research was funded by FAPESP-07/59757-2 (F.U.F. Lima).

References

Arblaster J M, Meehl G A. 2006. Contributions of external forcings to Southern Annular Mode trends. J Climate, 19(12): 2896–2905

Armstrong E M, Wagner G, Vazquez-Cuervo J, et al. 2012. Comparisons of regional satellite sea surface temperature gradients derived from MODIS and AVHRR sensors. Int J Remote Sens, 33(21): 6639–6651

Bonjean F, Lagerloef G S E. 2002. Diagnostic model and analysis of the surface currents in the tropical Pacific Ocean. J Phys Oceanogr, 32(10): 2938–2954

Brown E, Colling A, Park D, et al. 2001. Ocean circulation. 2nd edn. Amsterdam: Elsevier

Carleton A M. 2003. Atmospheric teleconnections involving the Southern Ocean. J Geophys Res, 108(C4): 8080. doi: 10.1029/2000JC000379

Carvalho L M V, Jones C, Ambrizzi T. 2005. Opposite phases of the Antarctic Oscillation and relationships with intraseasonal to interannual activity in the Tropics during the austral summer. J Climate, 18(5): 702–718

Chereskin T K, Roemmich D. 1991. A comparison of measured and wind-derived Ekman transport at 11°N in the Atlantic Ocean. J Phys Oceanogr, 21(6): 869–878

Chin T M, Milliff R F, Large W G. 1998. Basin-scale, high-wavenumber sea surface wind fields from a multiresolution analysis of scatterometer data. J Atmos Oceanic Technol, 15(3): 741–763

Chin T M, Vazquez J, Armstrong E M, et al. 2010. Algorithm theoretical basis document: multi-scale. Motion-compensated analysis of sea

surface temperature, Version 1.1. Washington DC: NASA.

Chin T M, Vazquez-Cuervo J, Armstrong E M. 2014. On "Gridless" interpolation and subgrid data density. J Atmos Oceanic Technol, 31(7): 1642–1652

Comiso J C, Gordon A L. 1998. Interannual variability in summer sea ice minimum, coastal polynyas and bottom water formation in the Weddell Sea//Jeffries M O. Antarctic sea ice: physical processes, interactions and variability. Washington DC: American Geophysical Union, 293–315

Cushman-Roisin B, Beckers J M. 2009. Introduction to geophysical fluid dynamics: physical and numerical aspects. Amsterdam: Academic Press, 789

Dash P, Ignatov A, Martin M, et al. 2012. Group for High Resolution Sea Surface Temperature (GHRSST) analysis fields inter-comparisons—Part 2: Near real time web-based level 4 SST Quality Monitor (L4-SQUAM). Deep Sea Res Part II Top Stud Oceanogr, 77–80: 31–43

de Lima F U F, Véspoli de Carvalho L M. 2008. Extreme intra-seasonal anomalies in the Amundsen and Bellingshausen sea-ice area, Antarctica, during the austral winter. Ann Glaciol, 48(1): 58–64

Fyfe J C, Saenko O A, Zickfeld K, et al. 2007. The role of poleward-intensifying winds on Southern Ocean warming. J Climate, 20(21): 5391–5400

Ghil M, Mo K. 1991. Intraseasonal oscillations in the global atmosphere. Part II: Southern Hemisphere. J Atmos Sci, 48(5): 780–792

Gillett N P, Thompson D W J. 2003. Simulation of recent Southern Hemisphere climate change. Science, 302(5643): 273–275

Glasser N F, Scambos T A. 2008. A structural glaciological analysis of the 2002 Larsen B ice-shelf collapse. J Glaciol, 54(184): 3–16

Gong D Y, Wang S W. 1999. Definition of Antarctic Oscillation index. Geophys Res Lett, 26(4): 459–462

Gordon A L, Georgi D T, Taylor H W. 1977. Antarctic polar front zone in the western Scotia Sea-summer 1975. J Phys Oceanogr, 7(3): 309–328

Gordon A L. 1981. Seasonality of Southern Ocean sea ice. J Geophys Res, 86(C5): 4193–4197

Gordon A L, Visbeck M, Huber B. 2001. Export of Weddell Sea deep and bottom water. J Geophys Res, 106(C5): 9005–9017

Haines S L, Jedlovec G J, Lazarus S M. 2007. A MODIS sea surface temperature composite for regional applications. IEEE Trans Geosci Remote Sens, 45(9): 2919–2927

Hall A, Visbeck M. 2002. Synchronous variability in the Southern Hemisphere atmosphere, sea ice, and ocean resulting from the Annular Mode. J Climate, 15(21): 3043–3057

Helms H D. 1967. Fast fourier transform method of computing difference equations and simulating filters. IEEE Trans Audio Electroacoust, 15(2): 85–90

Higgins R W, Kousky V E, Silva V B S, et al. 2010. Intercomparison of daily precipitation statistics over the United States in observations and in NCEP reanalysis products. J Climate, 23(17): 4637–4650

Holland P R, Kwok R. 2012. Wind-driven trends in Antarctic sea-ice drift. Nat Geosci, 5(12): 872–875

Jacobs S S, Amos A F, Bruchhausen P M. 1970. Ross sea oceanography and Antarctic bottom water formation. Deep Sea Res Oceanogr Abstr, 17(6): 935–962

Jia X L, Chen L J, Ren F M, et al. 2011. Impacts of the MJO on winter rainfall and circulation in China. Adv Atmos Sci, 28(3): 521–533

Jin D, Waliser D E, Jones C, et al. 2013. Modulation of tropical ocean surface chlorophyll by the Madden–Julian Oscillation. Climate Dyn, 40(1–2): 39–58

Jones C, Gottschalck J, Carvalho L M V, et al. 2011. Influence of the Madden-Julian oscillation on forecasts of extreme precipitation in the contiguous United States. Mon Wea Rev, 139(2): 332–350

Kara A B, Wallcraft A J, Metzger E J, et al. 2007. Wind stress drag coefficient over the global ocean. J Climate, 20(23): 5856–5864

Large W G, Pond S. 1981. Open ocean momentum flux measurements in moderate to strong winds. J Phys Oceanogr, 11(3): 324–336

Lau K M, Sheu P J, Kang I S. 1994. Multiscale low-frequency circulation modes in the global atmosphere. J Atmos Sci, 51(9): 1169–1193

Le Calvé O. 2002. Propriétés physiques du milieu marin. Un cours d'introduction à l'océanographie physique. Institut des Sciences de l'Ingénieur de Toulon et du Var. http://lecalve.univ-tln.fr/oceano/polycop/poly.pdf

Levitus S. 1987. Meridional Ekman heat fluxes for the World Ocean and individual ocean basins. J Phys Oceanogr, 17(9): 1484–1492

Madden R A, Julian P R. 1994. Observations of the 40-50-day tropical oscillation—A review. Mon Wea Rev, 122(5): 814–837

Mariano A J. 1990. Contour analysis: A new approach for melding geophysical fields. J Atmos Oceanic Technol, 7(2): 285–295

Mariano A J, Brown O B. 1992. Efficient objective analysis of dynamically heterogeneous and nonstationary fields via the parameter matrix. Deep Sea Res Part A Oceanogr Res Pap, 39(7–8): 1255–1271

Markus T, Kottmeier C, Fahrbach E. 1998. Ice formation in coastal polynyas in the Weddell Sea and their impact on oceanic salinity//Jeffries M O. Antarctic sea ice: physical processes, interactions and variability. Washington DC: American Geophysical Union, 273–292

Martinson D G, Iannuzzi R A. 1998. Antarctic ocean-ice interaction: implications from ocean bulk property distributions in the Weddell Gyre//Jeffries M O. Antarctic sea ice: physical processes, interactions and variability. Washington DC: American Geophysical Union, 243–271

Mitchell J F B, Hills T S. 1986. Sea-ice and the Antarctic winter circulation: A numerical experiment. Quarterly Journal of the Royal Meteorological Society, 112(474): 953–969

Mo K C, Paegle J N. 2001. The Pacific-South American modes and their downstream effects. Int J Climatol, 21(10): 1211–1229

Parkinson C L. 2004. Southern Ocean sea ice and its wider linkages: insights revealed from models and observations. Antarct Sci, 16(4): 387–400

Raphael M N. 2007. The influence of atmospheric zonal wave three on Antarctic sea ice variability. J Geophys Res, 112(D12): D12112

Rignot E, Casassa G, Gogineni P, et al. 2004. Accelerated ice discharge from the Antarctic Peninsula following the collapse of Larsen B ice shelf. Geophys Res Lett, 31(18): L18401

Rintoul S R, Hughes C, Olbers D. 2001. The Antarctic circumpolar current system//Siedler G, Gould J. Ocean Circulation and Climate. Amsterdam: Academic Press, 271–302

Saha S, Moorthi S, Pan H L. 2010. The NCEP climate forecast system reanalysis. Bull Amer Meteor Soc, 91(8): 1015–1058

Scambos T A, Bohlander J A, Shuman C A, et al. 2004. Glacier acceleration and thinning after ice shelf collapse in the Larsen B embayment, Antarctica. Geophys Res Lett, 31(18): L18402

Smith R C, Stammerjohn S E. 2001. Variations of surface air temperature and sea ice extent in the western Antarctic Peninsula region. Ann Glaciol, 33: 493–500

Spence P, Griffies S M, England M H, et al. 2014. Rapid subsurface warming and circulation changes of Antarctic coastal waters by poleward shifting winds. Geophys Res Lett, 41(13): 4601–4610

Streten N A, Pike D J. 1980. Characteristics of the broadscale Antarctic sea ice extent and the associated atmospheric circulation 1972–1977. Archiv Meteor Geophys Bioklimatol Sér A, 29(3): 279–299

Stroeve J. 2003. Sea ice trends and climatologies from SMMR and SSM/I-SSMIS. version 1. Boulder, Colorado, USA: NASA National Snow and Ice Data Center Distributed Active Archive Center

Thoma M, Grosfeld K, Lange M A. 2006. Impact of the Eastern Weddell Ice Shelves on water masses in the eastern Weddell Sea. J Geophys Res, 111(C12): C12010

Thomas D N, Dieckmann G S. 2003. Sea ice: an introduction to its physics, chemistry, Biology and geology. New York: Blackwell, 416

Thompson D W J, Solomon S, Kushner P J, et al. 2011. Signatures of the Antarctic ozone hole in Southern Hemisphere surface climate change. Nat Geosci, 4(11): 741–749

Tomczak M, Godfrey J S. 2003. Regional oceanography: an introduction. 2nd edn. Delhi: Daya Publishing House

Turner J, Pendlebury S. 2004. The international antarctic weather forecasting handbook. Cambridge: British Antarctic Survey, 663

Vaughan D G, Doake C S M. 1996. Recent atmospheric warming and retreat of ice shelves on the Antarctic Peninsula. Nature, 379(6563): 328–331

Vaughan D G, Marshall G J, Connolley W M, et al. 2003. Recent rapid regional climate warming on the Antarctic Peninsula. Climatic Change, 60(3): 243–274

Vazquez-Cuervo J, Dewitte B, Chin T M, et al. 2013. An analysis of SST gradients off the Peruvian Coast: The impact of going to higher resolution. Remote Sens Environ, 131: 76–84

Walsh J E. 1983. The role of sea ice in climatic variability: theories and evidence. Atmos Ocean, 21(3): 229–242

Weijer W, Sloyan B M, Maltrud M E, et al. 2012. The Southern Ocean and its climate in CCSM4. J Climate, 25(8): 2652–2675

Wunsch C. 1998. The work done by the wind on the oceanic general circulation. J Phys Oceanogr, 28(11): 2332–2340

Yelland M, Taylor P K. 1996. Wind stress measurements from the open ocean. J Phys Oceanogr, 26(4): 541–558

Yuan X J, Martinson D G. 2000. Antarctic sea ice extent variability and its global connectivity. J Climate, 13(10): 1697–1717

Zhang C D. 2005. Madden-Julian oscillation. Rev Geophys, 43(2): RG2003, doi: 10.1029/2004RG000158

Zwally H J, Comiso J C, Parkinson C L, et al. 2002. Variability of Antarctic sea ice 1979–1998. J Geophys Res, 107(C5): 9-1–9-19, doi: 10.1029/2000JC000733